1   **A Novel Nanotubular TiO₂-based Plug-Flow Reactor For Gas Phase Photocatalytic**

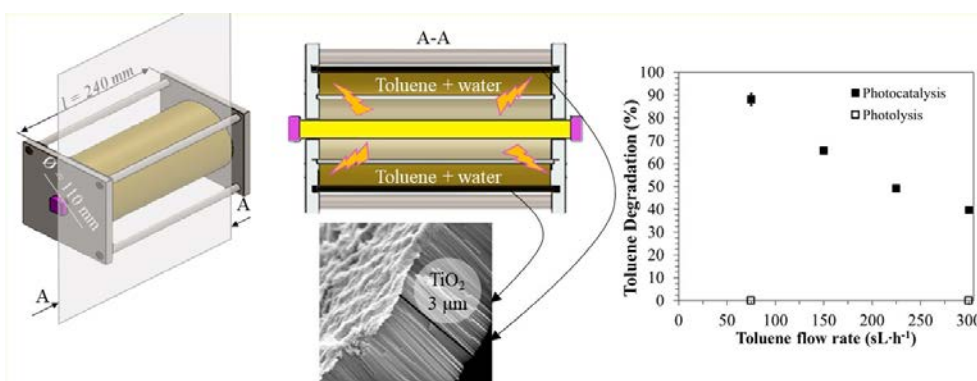2   **Degradation of Toluene**

3

4   Umberto Bellè[a], Marzio Invernizzi[b], Elisa Polvara[b], Andrea Lucotti[b], Maria Vittoria Diamanti[a,*],

5   Selena Sironi[b], MariaPia Pedeferri[a]

6

7   [a] Department of Chemistry, Materials and Chemical Engineering "G. Natta", Politecnico di Milano,

8   Via Luigi Mancinelli 7, Milan 20131, Italy

9   [b] Department of Chemistry, Materials and Chemical Engineering "G. Natta", Politecnico di Milano,

10   Piazza Leonardo da Vinci 32, 20133 Milan, Italy

11

12   [*]Corresponding author. Tel.: +39 02 2399 3137

13   E-mail addresses: mariavittoria.diamanti@polimi.it

14

15

16

17

18

19

20

21

Abstract:

In this study, a novel annular plug flow reactor (PFR) with built-in nanotubular TiO_2 obtained via anodizing was tested for the photocatalytic degradation of toluene. The oxide was grown directly on a titanium substrate by anodizing, as this method implies no risk of nanoparticles release in the environment during or after the photocatalytic process. Experiments were carried out in presence of an UV-A light source by modulating relative humidity, gas concentration and flow rate, to evaluate possible applications in indoor and industrial environments.

The photocatalytic system demonstrated high photodegradation efficiency up to 90% for an inlet toluene concentration of 10 ppm, thus showing potential applications in mildly polluted environments, such as homes, offices and up to more severely polluted ones like offset printing plants, automobile manufacturing industries or even professional kitchens, where the exposure to cooking oil fumes is significant. In case of high toluene concentration, the initial degradation percentage falls in a range between 60 and 70%; subsequently, the instant degradation shows a gradual decrease ascribed to photocatalyst deactivation, which occurred due to the accumulation of recalcitrant by-products on the adsorption sites, thus highlighting some limitations for industrial applications when selected VOCs are present; nonetheless, the photocatalyst regained its initial activity through a simple photocatalyst reactivation process, leading to a maximum instant degradation percentage up to 90% for an inlet toluene concentration of 20 ppm.

48

Highlights:

- Immobilized, high surface area TiO_2 films were obtained via anodizing

- A plug-flow reactor for gas-phase photocatalysis was developed

- A high degradation efficiency was achieved for medium-low toluene concentration

- Photocatalyst deactivation was recovered through a simple reactivation

54

55

56

57

58

59

60

61

62

63

64

65

66

67

68

69

70

71

72

73

74   1. INTRODUCTION

75   In the current industrialized society, air pollution represents one of the biggest concerns due to its

76   negative effects on human health, going from discomfort to serious respiratory diseases; long-term

77   exposures - particularly in strongly polluted industrial environments - can also induce cancers or

78   severe forms of intoxication [1–3]. Air pollution has a negative impact even on the environment,

79   being the cause of hazardous effects such as acid rains and ozone depletion. Indeed, it is indisputable

80   that pollution due to industrialization is one of the main factors of global warming and climate change

81   [4–7].

82   Among air pollutants, Volatile Organic Compounds (VOCs) are of particular interest being one of

83   the major sources of pollution in both indoor and outdoor environments and responsible for several

84   adverse effects on human health and ecosystem; specifically, compounds like toluene, benzene,

85   ethylbenzene and xylene (so called BTEX) have been found to be carcinogenic to humans [8–11].

86   Several methods for VOCs abatement have been developed, such as the use biofilters, adsorption,

87   absorption or catalytic oxidation [12–16]; nevertheless, these technologies may involve side effects

88   and further treatments, increasing the cost of the abatement process.

89   Advanced Oxidation Processes (AOPs) such as ozonation, photocatalysis and photo-Fenton are

90   promising technologies for the abatement of VOCs both in indoor and in outdoor environment;

91   particularly, heterogeneous photocatalysis is one of the most studied AOPs since it allows to exploit

92   solar energy for accelerating the degradation of organic pollutants, possibly leading to full

93   mineralization. Titanium dioxide (TiO_2) photocatalysis has gained particular attention, as its bandgap

94   properties (3.2 eV in its widely employed anatase phase) and the high conductivity of the

95   photogenerated charges allow a high photodegradation efficiency under ambient temperature and

96   pressure conditions [17–21].

97   Most studies are conducted by using either TiO_2 nanoparticles, or by immobilizing them in the form

98   of thin film applied on substrates such as glass or steel [8,10,22,23]; although the use of TiO_2-based

99   films allows to avoid recovery issues typical of nanoparticles dispersed in aqueous media or released

100 in air, where recovery is impossible and hazards would overcome benefits, particles agglomeration

101 and deterioration of the films adherence on the substrate generally limit photocatalytic efficiency and

102 possibly pose some health issues. Therefore, the generation of stable nanostructured TiO_2 layers with

103 a high surface area for promoting the degradation of pollutants on the photocatalyst surface is

104 desirable.

105 This can be achieved through anodic oxidation, which grows well-ordered self-organized nanotubular

106 (NT) TiO_2 arrays strongly immobilized on titanium; by imposing a cell voltage between the anode

107 (i.e. the titanium substrate) and a conductive cathode in a fluoride containing organic electrolyte, it is

108 possible to obtain an oxide with high specific surface area and reproducible and controlled

109 morphology [20,24–26].

110 To date, several studies have been focused on the photocatalytic properties of TiO_2 NTs for the

111 degradation of pollutants in liquid phase [27–30]; however, their application for air purification has

112 been studied to a limited extent, and the size of the photocatalyst is generally restricted, being limited

113 to small laboratory samples (e.g., 1 x 1 cm^2) [31–33]. In fact, TiO_2-based photocatalysts for annular

114 reactor systems are produced by using hydrothermal synthesis or other coatings based on TiO_2

115 powders, whose limits fall mostly in the risk of release of TiO_2 nanoparticles in the environment. This

116 implies that mass loss leads to a decrease in photocatalytic degradation percentage over time; on the

117 opposite, the strong stability of self-organized TiO_2 arrays obtained via anodization, together with

118 their large surface area and their geometry that enhances both photogenerated charge transfer and UV

119 UV absorption over the tube, leads to high photoactivity in short and long term and high reliability

120 of the system also for prolonged use [26,30, 34–39].

121 Moreover, the dimensions of the reactors are often limited, and few studies have been carried out on

122 annular PFR having a reaction chamber of about 1000 cm^3 [40–42]. At the same time, reaction

123 chamber radius is always very small, as an increase of its diameter leads to a decrease of the contact

124 time between gas and photocatalyst surface as well as a reduction in light intensity reaching the

125 photocatalyst surface, thus limiting the efficiency of the photocatalyst [43,44].

126 An assessment of the photocatalytic properties of nanotubular structures in full-size devices for both

127 indoor and outdoor environments (particularly industrial ones) is therefore still missing, while being

128 fundamental for evaluating possible real and large-scale applications.

129 In this work, an analysis of the photocatalytic properties of self-assembled TiO_2 NTs for the

130 photodegradation of toluene is proposed. The experiments have been carried out by using an annular

131 PFR reactor in which the photocatalyst entirely covers the inner wall of the reactor, with an overall

132 surface area exposed of 1040 cm^2. This reactor is characterized by a reaction chamber of

133 approximatively 1200 cm^3, with a distance between the inner and outer tube of 4 cm. Photoactivation

134 is achieved by UV-A radiation. Toluene photodegradation has been monitored in continuous by

135 analysing concentration variation with a photoionization detector (PID). The effects of relative

136 humidity, inlet gas concentration and flow rate on the photocatalytic performance of the PFR reactor

137 were evaluated, to investigate potential applications in indoor home and industrial environments.

138 The PFR reactor allows to use TiO_2 NTs-based photocatalyst, generally used for the degradation of

139 dyes or other organic pollutants in liquid phase in batch reactors, in continuous mode, which is a more

140 realistic situation that involves a possible use for the abatement of pollutants in real systems.

141

142 2. MATERIALS AND METHODS

143

144 2.1. Photocatalyst production and characterization

145 Tests with PFR reactor were performed by introducing in the reactor chamber ten interlocked

146 anodized and annealed titanium meshes, each 320 x 25 mm^2 wide and 0.5 mm thick.

147 First of all, each commercially pure grade 2 ASTM titanium mesh was cleaned by sonication in EtOH

148 for 10 minutes, then anodized in ethylene glycol (EG) + 0.2 M NH_4F + 2 M H_2O at 45 V for 30 min

149 in potentiostatic conditions (Potentiostat LTC-Caoduro), according to previous studies [30]; all

150 chemicals were purchased from Sigma-Aldrich (analytical grade).

151 Smaller samples (2.5 x 2.5 cm^2) were anodized with the same procedure, starting from both a grade

152 2 titanium sheet polished with P600 SiC paper and a portion of the same mesh used for the larger

153 samples. Such samples were then used for a preliminary evaluation of substrate effect.

154 After the anodization process, both larger meshes and smaller samples were carefully rinsed with

155 distilled water, dried with air stream and then subjected to annealing treatment in a GEFRAN 1200

156 oven at 500 °C for two hours to induce the crystallization of the amorphous oxide layers obtained

157 through anodizing.

158 Scanning Electron Microscopy (SEM) analyses were performed with an EVO Series 50 (Carl Zeiss

159 AG, Oberkochen, Germany), and ImageJ software (version 1.52t) was used for image processing. X-

160 Ray Diffraction (XRD) analyses were performed with an Empyrean diffractometer (Malvern

161 Panalytical, Malvern, UK), using CuK$_\alpha$ and CuK$_\beta$ radiations.

162

163 2.2. Preliminary photocatalytic tests in liquid phase

164 The photoactivity of TiO$_2$ nanotubular arrays grown on titanium mesh was initially tested in liquid

165 phase and compared with the one of TiO$_2$ NTS grown on titanium foils, already analyzed in previous

166 studies [30,45]. A batch reactor containing an aqueous solution of the organic dye Rhodamine B

167 (RhB) as target pollutant and UV-A radiation was used, as described in a previous work [30]. Dye

168 absorbance variation was evaluated with a spectrophotometer SPECTRONIC 200E (Thermo Fisher

169 Scientific, Les Ulis, France). Tests were performed over three hours, with absorbance measurements

170 performed every 30 min; the reaction rate constant k$_{app}$ was evaluated according to a pseudo-first-

171 order Langmuir–Hinshelwood kinetic model [30,45]:

172

173 $$\ln\left(\frac{C}{C_0}\right) = -k_{app}t \qquad\qquad (1)$$

174

175 where C is the dye concentration at time t and C$_0$ is the initial RhB concentration; both C and C$_0$

176 values were derived from absorbance measurements by using Beer-Lambert law.

177 Each test was performed three times to ensure good reproducibility of the results, whereas adsorption

178 tests by dark storage and photolysis test were also performed to evaluate possible side effects; the

179 effects of both adsorption in dark and RhB photolysis were considered negligible due to the small

180 absorbance variation with respect to photocatalytic degradation test in presence of both types of

181 photocatalysts (see Supplementary Material, Figure S1).

182

183 2.3. Annular PFR reactor design

184 Photocatalytic tests in gas phase were performed in an annular PFR reactor. The design of the reactor

185 was performed using SOLIDWORKS (version 2020 SP5) and includes a cylindrical pipe enclosed

186 by two flanges in which 3 pneumatic connections for gas inlets and outlets are located on each flange,

187 respectively. The airtightness of the reactor is guaranteed by the presence of four lateral threaded bars

188 with knobs to help screwing. Pipe, bars and flanges are made in Al alloy (Anticorodal Al alloy 6000)

189 (see Supplementary Material, Figure S2).

190 Photoillumination was provided by an UV-A Philips Actinic BL TL-D 15W10 1SL/25 lamp, axially

191 positioned inside the PFR, resulting concentric with respect to the aluminum pipe (Figure 1 and

192 Figure S3). Its emission spectrum falls between 350 and 400 nm, with a strong emission peak at 365

193 nm. A borosilicate pipe was positioned between the UV-A lamp and the external Al pipe in order to

194 both protect the lamp from any possible contamination of environment and to avoid gas leaking

195 through the inlet holes of the lamp in the reactor (Figure 1). Borosilicate glass was selected since it

196 guarantees a high transmittance of UV-A radiation above 345 nm [46,47], a necessary condition for

197 the photoactivation of TiO_2.

198

199

200
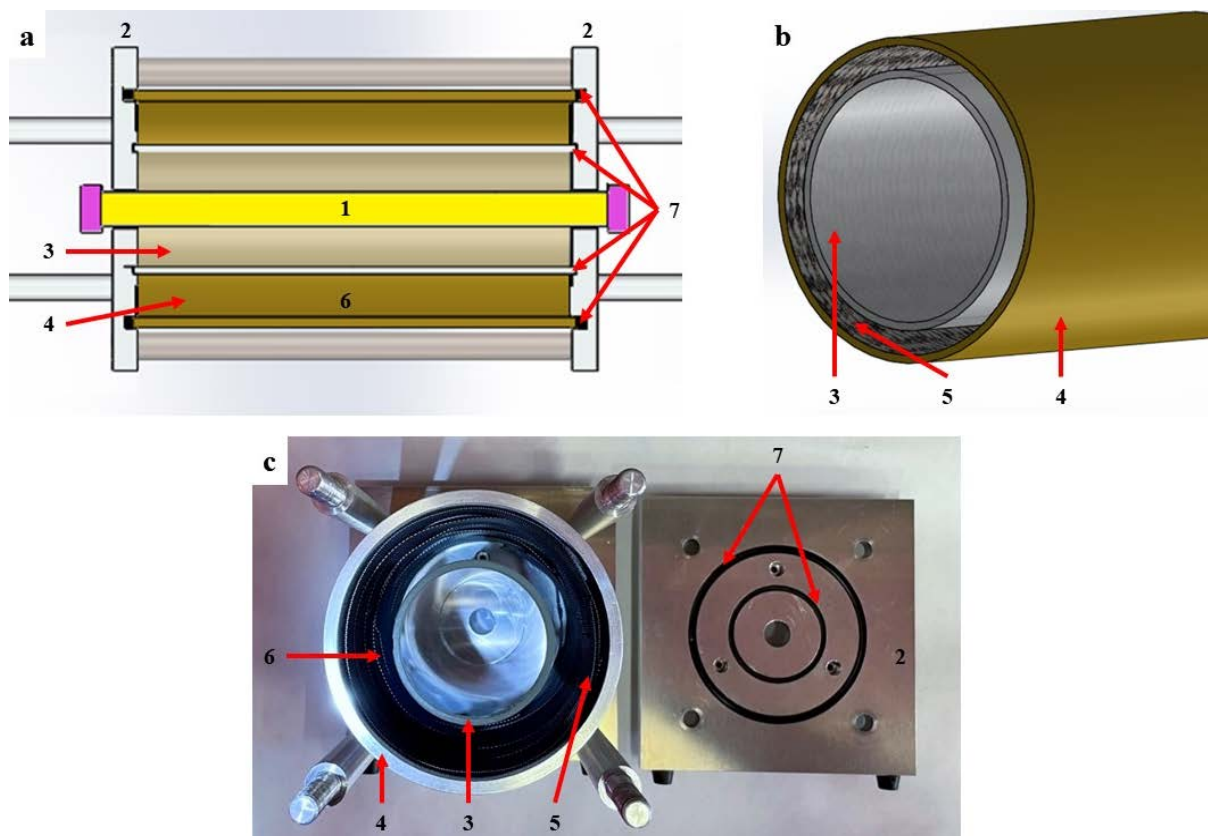
Figure 1. (a) Horizontal cross-section of the annular PFR reactor designed with SOLIDWORKS; (b) Vertical cross-section of the annular PFR reactor designed with SOLIDWORKS; (c) Vertical cross-section of the manufactured annular PFR reactor. Keys: (1) UV-A lamp (in yellow) and its electrical connection (in violet); (2) Inlet and outlet Al flanges with three screwed pneumatic connections for inlet channels; (3) Borosilicate pipe; (4) External Al pipe; (5) Photocatalyst; (6) Reaction chamber; (7) Butyl rubber O-Rings.

The profile of UV-A light intensity was evaluated through a Konica-Minolta UV Radiometer UM-10 (see Supplementary Material, Figure S4). A stable UV-A intensity was reached 15 seconds after its turning on, ensuring that toluene concentration variations were not affected by UV-A intensity variations.

The reaction gas flows between the inner borosilicate and outer Al pipe, i.e. in the reaction chamber, whose volume is approximately 1200 cm^3. The photocatalyst, consisting of the anodized and annealed mesh, was manually inserted in the inner wall of the outer Al pipe (Figure 1).

214 For each flange, two O-Rings in butyl rubber were positioned (one between the flange and the Al

215 pipe and the other between the flange and the borosilicate tube) to avoid possible gas leaks (Figure

216 1).

217 Details of reactor geometry are summarized in Supplementary Material, Table S1.

218

219 2.4. Photocatalytic tests in gas phase

220 The carrier gas in this study is synthetic air. Distilled water was used for controlling the relative

221 humidity of the inlet gas in the PFR reactor. Toluene was purchased from Sigma-Aldrich (analytical

222 grade); all experiments were performed at room temperature (24 ± 2 °C) under ambient pressure

223 conditions.

224 The apparatus used is schematized in Figure 2; all the tubing system was in PTFE ($Ø = 6$ mm) to

225 minimize toluene adsorption.

226
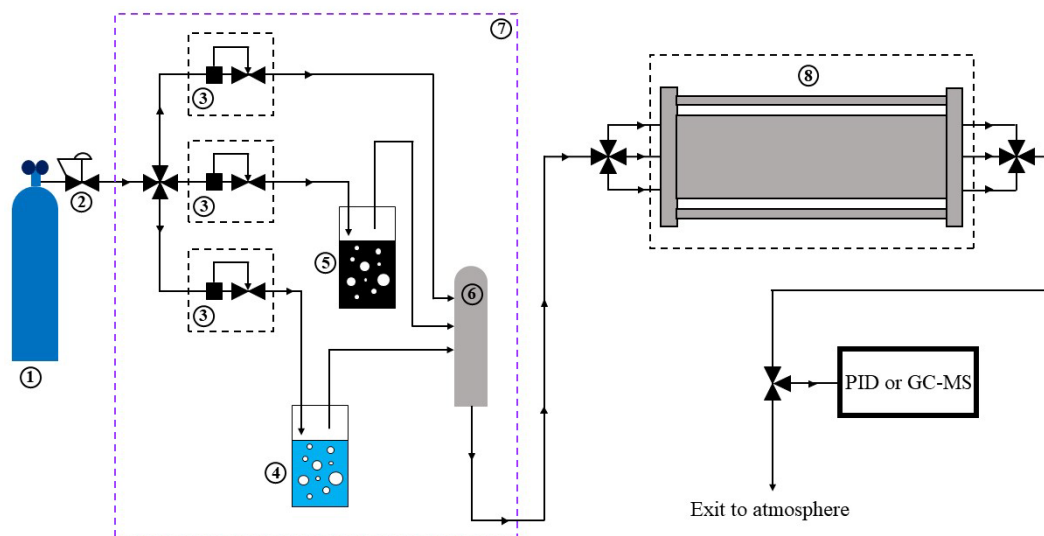
227

228 Figure 2. Flow sheet of the experimental apparatus used for photocatalytic degradation tests. Keys:

229 (1) Synthetic air source; (2) Shut-off valve; (3) Mass flow controllers; (4) Water vapor saturator; (5)

230 Toluene saturator; (6) Manifold (Gas mixing chamber); (7) Temperature-controlled confined

231 chamber; (8) PFR photocatalytic reactor.

232

233 Synthetic air coming from the compressed air line is initially divided into three secondary streams,

234 each one managed through a mass flow controller (MC ALICAT Scientific). Two of these secondary

235 lines are employed for vaporizing both toluene and water through saturators. Once water vapor and

236 toluene streams are generated, these are mixed with synthetic air in the manifold to provide the reactor

237 feed of both desired toluene concentration and relative humidity and total inlet airflow rate in the PFR

238 reactor. The mass flow control system and saturators were posed in a temperature-controlled confined

239 chamber (violet box in Figure 2); temperature was kept constant and verified at the beginning and at

240 the end of each experiment accordingly. Humidity in the inlet flow was varied by changing dry air

241 and water bubbler flow ratio. Humidity was checked at the manifold outlet via a thermohygrometer

242 (Thermohygrometer Testo 605i).

243 The so obtained reaction mixture was passed through three input channels into the reaction chamber,

244 and then collected by three output channels, in turn conveyed into a single outlet channel. In

245 preliminary studies, tests were carried out to both verify the integrity of the reactor and to assess the

246 distribution of the three inlet gas flows inside the reaction chamber, which resulted homogeneously

247 redistributed with no leaks.

248 In a typical test, the system is left to reach the equilibrium for 15 minutes until the toluene

249 concentration results constant in a range [Toluene]$_{inlet}$ $\pm$ 1 ppm. The flow stream is then passed

250 through the dark PFR reactor (absence of UV radiation) until the concentration equilibrium is

251 established; this process allows to verify the presence of possible adsorption phenomena on the

252 photocatalyst surface. Before each photocatalysis test, adsorption tests were carried out for 30

253 minutes, and in all the analyzed cases the inlet-outlet flow equality was reached in two minutes and

254 maintained for the following 28 minutes. Hence, whenever toluene concentration decreased when

255 switching on UV-A irradiation, these variations could be ascribed to the only action of light and

256 photocatalyst, discarding possible adsorption effects.

257 Indeed, once the equilibrium was reached, the UV-A lamp was turned on and the gas concentration

258 variation was sampled continuously by using a portable 10.6 eV PID detector (PID Tiger - Ion Science

Italia s.r.l). Tests under irradiation were performed in a range of 30 – 360 minutes. After each experiment, the toluene stream was stopped and the reactor was flushed for 60 minutes using synthetic air and high relative humidity (between 50% and 75%), leaving the UV-A lamp turned on to favor the removal of possible adsorbed byproducts, followed by dry air to remove any residual moisture from the photocatalyst surface.

Control experiments were conducted by using an external Al pipe without photocatalyst to estimate possible background photolysis phenomena; tests were performed for 30 minutes, and results showed that toluene photolysis can be considered negligible (see Supplementary Material, Figure S5).

In specific cases, the outlet gas stream was also examined by gas chromatography (TD-GC-MS) to evaluate the presence of possible photocatalytic degradation by-products. Sampling was performed at the end of dark equilibrium and in presence of UV-A radiation, after 2 and 30 minutes irradiation. CO_2 determination in the outstream gas was also performed with a NDIR sensor (MRU Optima7 BioGas). Eventually, possible mineralization residues present on NTs films were searched via Fourier transform infrared (FT-IR) spectroscopy. The micro-FT-IR spectra were recorded in reflection mode on the anodized mesh through a 15x Cassegrain objective (numerical aperture NA = 0.58) with a Nicolet Nexus 670 FT-IR spectrometer (4 cm^{-1} resolution, Thermo Fisher Scientific, Les Ulis, France) coupled with a Thermo Electron Continuµm IR microscope.

The photocatalytic VOC degradation was measured as follows:

$$\text{Photocatalytic VOC efficiency (\%)} = \frac{(C_0 - C_i)}{C_0} \times 100 \tag{2}$$

where C_t is dye concentration at time instant i and C_0 is inlet concentration.

The amount of degraded mass was evaluated as:

$$\text{Degraded VOC mass (mg)} = MW_{VOC} \int_0^t [C_{in} - C(i)] \cdot Q \cdot di \tag{3}$$

284

285 where MW_{VOC} is VOC molecular weight, t is test duration, C_{in} is inlet concentration, $C(i)$ is outlet

286 concentration at instant time i and Q is inlet flow rate.

287 In case of low toluene concentrations, the kinetic model was evaluated. By assuming a Langmuir-

288 Hinshelwood model (L-H) for the description of adsorption-desorption phenomena and surface

289 reactions if the mass transfer is not the limiting step [48], the reaction rate at the equilibrium can be

290 written as:

291

292 $$r = k\theta_a = k\frac{K_{LH}C}{1+K_{LH}C} \tag{4}$$

293 where r is reaction rate, k is kinetic constant, θ_a is pollutant surface coverage, K_{LH} is Langmuir-

294 Hinshelwood adsorption equilibrium constant and C pollutant concentration.

295 By considering that the characteristic equation for a PFR reactor is:

296

297 $$r = -\frac{dC}{d\tau} \tag{5}$$

298 where τ is the residence time, the characteristic equation for a PFR reactor in which L-H model can

299 be written results by combination of Eq. (4) and Eq. (5):

300

301 $$\frac{dC}{d\tau} = -k\frac{K_{LH}C}{1+K_{LH}C} \tag{6}$$

302

303 By rearranging an integrating Eq. (6), the following can be obtained:

304

305 $$\frac{\ln(C_{in}/C_{out})}{(C_{in}-C_{out})} = k_{app}\frac{\tau}{(C_{in}-C_{out})} - K_{LH} \tag{7}$$

306

307 where C_{in} is inlet concentration, C_{out} is outlet concentration when the PFR reactor reaches stability,

308 and k_{app} is pseudo-first-order reaction rate constant ($k_{app} = k \cdot K_{LH}$).

309 By considering low toluene concentrations ($K_{LH}C \ll 1$), Eq. (7) can be simplified and written as:

310

311 $$\ln\left(\frac{C_{out}}{C_{in}}\right) = -k_{app}\tau \qquad (8)$$

312

313 Eq. (8) allows to evaluate the reaction rate constant according to a pseudo-first-order Langmuir–

314 Hinshelwood kinetic model, similarly to Eq. (1) for the batch reactor.

315 Thus, by varying the inlet flow rate it is possible to evaluate both the kinetics of the process and the

316 validity of L-H model for low pollutant concentrations.

317 With the previously described gas-phase setup, the effects of three different parameters, namely

318 relative humidity (RH), pollutant concentration and flow rate, on the photodegradation efficiency and

319 kinetics were investigated. RH was varied from 0 to 75%. Inlet toluene concentration was in the range

320 between 10 and 80 ppm. The inlet flow rate varied from 75 sL/h to 300 sL/h. Residence times τ were

321 calculated as ratio between reaction chamber volume and flow rate. The evaluated conditions are

322 summarized in Table 1.

323

324 Table 1. List of evaluated conditions. Conditions * were repeated after an intensive cleaning cycle.

VOC	Concentration (ppm)	Flow rate (sL/h)	τ (s)	RH (%)
		75	57	
	10	150	28	50
		225	19	
		300	14	
Toluene				25*
	20	150	28	50*
				75*
				25
	30	150	28	50

			75
35	150	28	50
80	150	28	50

To investigate photodegradation kinetics, experiments were performed by irradiating the photocatalyst for 30 minutes at fixed concentration (10 ppm) and RH (50%) and by varying the inlet flow rate between 75 and 300 sL/h. Each test was repeated twice.

To investigate catalyst deactivation, a second series of tests was conducted at different toluene concentration for a period of 360 min at fixed flow rate (150 sL/h).

To investigate the effect of relative humidity, experiments were conducted by varying the relative humidity (0 %, 25 %, 50 % and 75 %) at two different toluene concentrations (20 and 30 ppm) under 120 min of UV-A irradiation. In all these tests, the flow rate was kept constant at 150 sL/h.

Lastly, the effect of re-activation of the photocatalyst was evaluated by performing tests at fixed toluene concentration (20 ppm) and fixed flow rate (150 sL/h) after an intensive cleaning cycle. This was performed by flushing synthetic air at high relative humidity (between 50% and 75%) and leaving the UV-A lamp turned on for 24 hours, in order to ensure a deep removal of any possible byproducts adsorbed on the photocatalyst surface.

Reyonolds numbers (Re) were calculated for the evaluated flow rate range (75 – 300 sL/h). Being Re in a range 28 – 111, the flow was considered laminar since in all cases Re was largely lower than 2100. Although the fluid regime is laminar, the high flow rates used allows to hypothesize that there are none mass transport limiting phenomena [4,33].
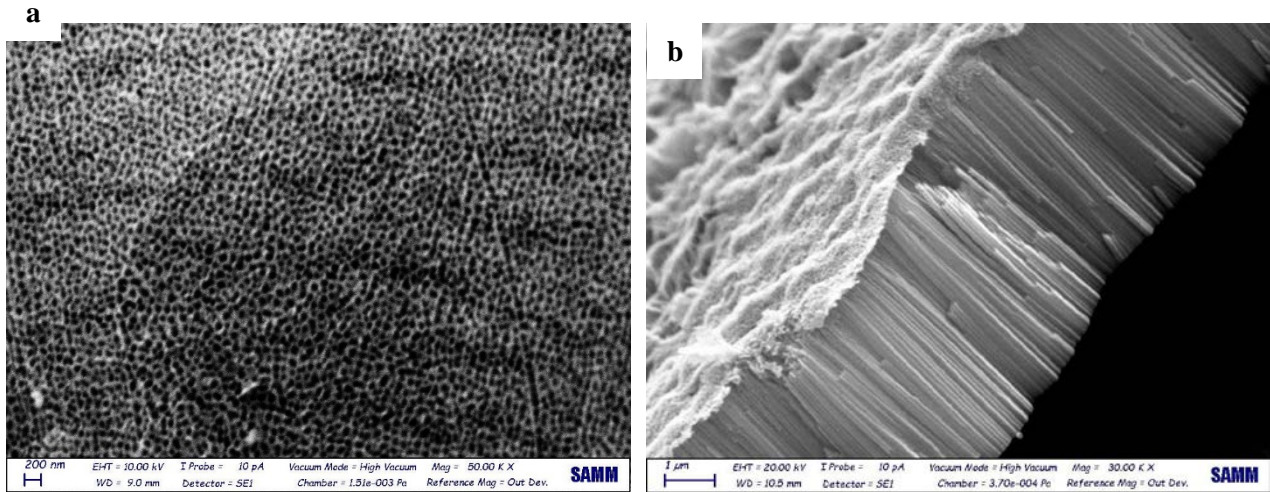
3. RESULTS AND DISCUSSION

3.1. Oxide characterization

348   SEM analyses were performed to ensure the formation of a proper nanotubular titanium dioxide

349   morphology. Figure 3 shows the top-view and cross-sectional images of the oxide after mesh

350   anodization.

351

352

353   Figure 3. SEM analyses of the TiO_2 oxide on mesh after anodization. (a) Top-view. (b) Cross-

354   sectional view.

355

356   A nanotubular morphology was formed, with average diameter of the tubes equal to 95 ± 5 nm and

357   average length of 4.5 ± 0.2 μm, similar to the morphology of nanotubes grown on titanium foil having

358   average diameter equal to 96 ± 6 nm and average length of 4.4 ± 0.3 μm according to previous work

359   [30]. These results show that the process was not affected by the different substrate shape.

360   Figure 4a shows XRD analyses performed on an anodized titanium mesh sample before and after the

361   annealing treatment at 500 °C.

362

363
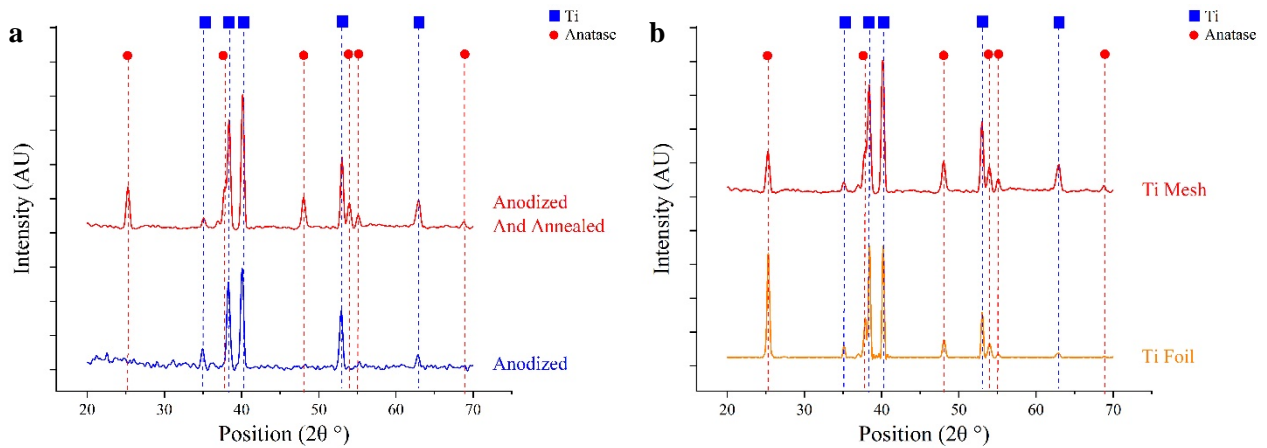
Figure 4. (a) XRD analyses of anodized Ti before (blue) and after (red) annealing treatment. (b) XRD

analyses of annealed on Ti foil (orange) and Ti mesh (red).

Results show that the as-anodized oxide is amorphous, while anatase peaks appear only after the

annealing treatment.

Moreover, a strong predominance of the anatase crystal phase of TiO2 was observed; rutile is present

in small traces, hardly detectable in the spectra.

A strong presence of anatase is considered favorable for the photocatalysis process, since this

crystalline phase has a higher electronic conductivity and a longer charge-carrier lifetime than rutile,

thus favoring the generation of strongly oxidizing radicals [49,50].

By comparing XRD spectra of calcinated oxide layers grown on the mesh and on the sheet (Figure

4b), no peak shifts were detected, suggesting that no relevant internal stresses are present in the oxide

grown on the mesh. Anyway, it is possible to notice that there is a considerable difference in terms

of peak intensity; this was ascribed to the fact that TiO_2 NTs grow perpendicularly on the Ti foil

surface, whereas in the mesh there is a bending of NTs growing directions due to the curved surface

at local level; consequently, a slight reduction in anatase peaks grown on mesh was recorded.

383   3.2. Preliminary photocatalytic tests in liquid phase

384   The preliminary comparison of photocatalytic activity of TiO_2 NTs grown on Ti mesh and Ti sheet

385   was performed by analyzing the degradation of RhB aqueous solutions (10^{-5} M) both in presence and

386   in absence of solution stirring in turbulent regime (400 rpm).

387   After 3 hours irradiation, RhB is degraded by almost 80% on titanium foils in presence of stirring,

388   reaching a quasi-complete discoloration (100% removal) for Ti mesh; on the opposite, stirring-free

389   tests provided lower photodegradation efficiency, that are 50% and 26% for NTs grown on mesh and

390   foil, respectively.

391   Figure 5 reports the pseudo-first-order kinetics of the evaluated conditions, according to Eq. (1). Dark

392   adsorption and photolysis tests provided negligible RhB concentration variations, confirming the

393   abovementioned photodegradation is fully related to the TiO_2 layers photocatalytic activity (see

394   Supplementary Material, Figure S1).

395
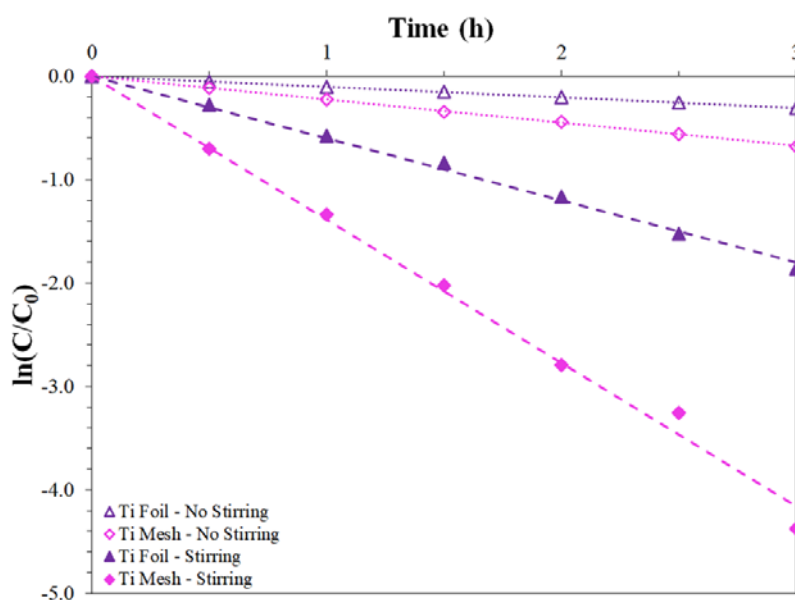
397   Figure 5. Pseudo-first-order kinetics of the RhB photocatalytic degradation process.

398

399 The excellent data linearity in semi-logarithmic scale confirms that RhB photodegradation follows

400 with a good approximation a pseudo-first-order kinetic model based on L-H adsorption mechanism,

401 evaluated by applying Beer-Lambert law.

402 In conclusion, substrate morphology seems to strongly affect photocatalytic reaction kinetics (see

403 Supplementary Material, Figure S6), with a reaction rate constant almost doubled with respect to the

404 foil samples (1.7 times).

405 A first explanation can be provided by analyzing the exposed surface area; in fact, even if the

406 geometrical area of both Ti mesh and Ti sheet is equal (2.5 x 2.5 cm^2) and the morphology of the

407 nanostructured oxide layer comparable, foils have an exposed surface area coincident with their

408 geometrical area (6.25cm^2), whereas for the mesh this assumption is no longer true. By assuming that

409 a mesh is made of braided strands having cylindrical shape, and by assuming that only half of the

410 cylindrical surface is exposed to UV radiation, the exposed surface area of the mesh was evaluated to

411 be approximately 30% larger than the one of the foil can be evaluated as:

412

413 Mesh exposed surface area $= L_{strand} \cdot d_{strands} \cdot \pi/2$ (9)

414

415 being L_{strand} and $d_{strands}$ the sum of lengths of all strands present in a unit surface of the mesh and the

416 strend diameter, respectively.

417 By considering a 6.25 cm^2 mesh sample with L_{strand} equal to 73.22 cm and by considering $d_{strands}$ equal

418 to 700 μm (according to SEM measurements), the exposed surface area is equal to 8.06 cm^2, that is

419 1.29 times higher that the foil ones.

420 Indeed, this is not sufficient to explain 1.7 times increase in reactivity. This can be ascribed to the

421 fact that a higher NTs density is present on mesh samples due to branching phenomena when tubes

422 grow on non-planar surfaces [51–53]; this allows both a higher dye adsorption and a better UV-A

423 harvesting, leading to an increase in photoactivity.

424   For these reasons, TiO$_2$ NTs grown on Ti mesh were selected for the photocatalytic degradation of

425   gas-phase pollutants in our custom-developed reactor.

426

427   3.3. Photocatalytic degradation of gas-phase pollutants

428   3.3.1. Low concentration

429   Degradation of low-concentrated toluene in the annular photoreactor chamber was evaluated by

430   fixing relative humidity (RH = 50%) and pollutant concentration (10 ppm) and by varying inlet flow

431   rate.

432   As discussed in Section 2, initial control tests were performed in absence of photocatalyst in order to

433   estimate the photolysis rate; moreover, before each test, toluene adsorption in dark was evaluated for

434   30 minutes for evaluating possible background effects. Concentration was constantly recorded as a

435   function of reaction time for 30 minutes in dark storage and subsequently, for the next 30 min under

436   UV-A illumination. Results show that both rates can be considered negligible, thus concentration

437   decrease in PFR reactor can be attributed exclusively to photocatalytic degradation.

438   Toluene concentration and degradation (%) profiles are shown in Figure 6. The solid line at time 0

439   highlights photocatalyst activation starting time, whereas negative time scale represents the 30

440   minutes equilibration time in absence of UV radiation. Concentration at time 0 was used as the inlet

441   concentration C$_0$ for the evaluation of both toluene conversion and photodegradation kinetics.

442

443
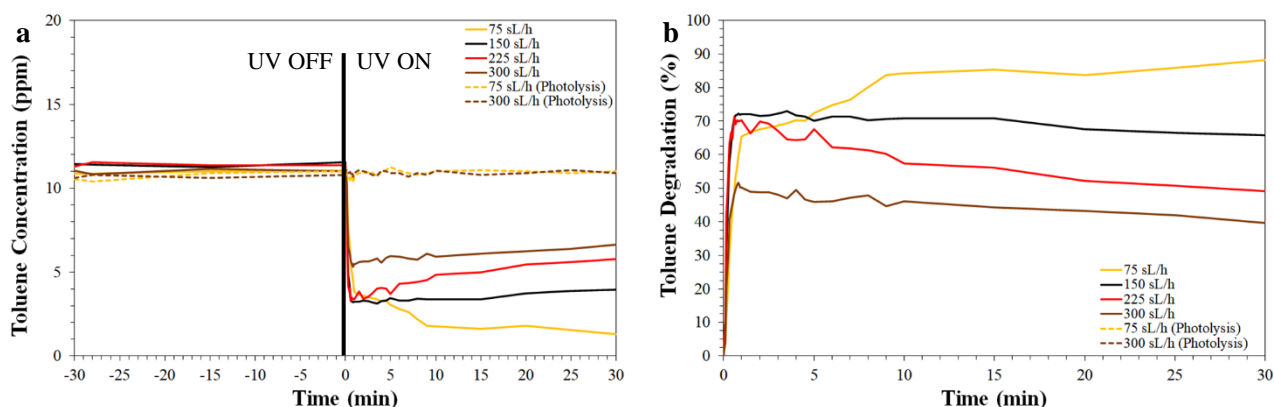
Figure 6. (a) Toluene concentration profile before and during UV-A irradiation (a) and toluene percent degradation (b).

Results show that concentration profile remains almost constant in dark environment (Figure 6a); once the UV-A lamp is turned on, a sharp toluene concentration decrease is measured in the first two minutes, revealing that the system provides an immediate response. As the photocatalytic process goes on, toluene concentration slightly increases. The only exception is represented by experiments performed at 75 sL/h, where the profile continuously decreases for the first 10 minutes after light ignition, and then stabilizes in a range of 2 ± 0.5 ppm.

Figure 6b shows the toluene conversion profile, and it is possible to see that maximum efficiency is reached in the first two minutes, reaching a degradation up to 70% for experiments performed at 150 and 225 sL/h. As the experiment proceeds, the toluene conversion rate gradually decreases till a pseudo-steady state is reached, thus implying a photocatalytic efficiency slightly decreasing over time. Indeed, the accumulation of possible by-products formed in the initial stage on the photocatalyst surface may compete with toluene adsorption on the photocatalyst, thus decreasing photoactivity. On the other hand, for very low flow rate (75 sL/h) gas recirculation occurs much more slowly and photodegradation and desorption of adsorbed byproducts is favored, while residence time increases ensuring longer contact times of toluene molecules with the surface. The effect of flow rate (and therefore residence time) on photoconversion efficiency is analyzed in more details in Figure 7.

As expected, toluene conversion increases as flow rate decreases (or as residence time increases). In particular, photocatalytic degradation percentage passes from 40% (flow rate equal to 300 sL/h) to 90% (flow rate of 75 sL/h) as τ increases. This behavior was ascribed to the fact that an increase in contact time between pollutant and photocatalyst favors its adsorption on the photocatalyst surface, as well as possible byproducts desorption, as previously mentioned.

On the other hand, an evaluation of total degraded toluene mass was performed by applying Eq. (3).

469   Figure 8 clearly shows that degraded mass profiles are strongly affected by the inlet flow rate, and

470   that the total amount of degraded mass increases as flow rate increases.

471
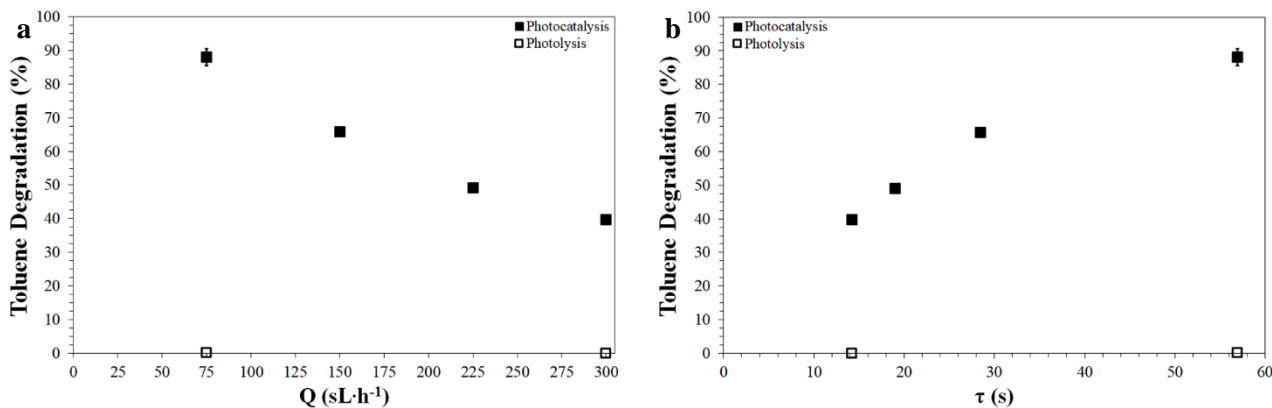
472

473   Figure 7. Toluene conversion as function of inlet gas flow rate (a) and residence time (b)

474

475   This can be ascribed to the fact that, by fixing the inlet concentration, the amount of pollutant (in

476   mass) entering the reaction chamber increases as the flow rate increases. Therefore, percentages

477   shown before are just a portion of the puzzle: although low flow rates allow an almost complete

478   degradation of the whole amount of pollutant introduced in the chamber per unit time, this amount is

479   lower than the quantity of pollutant introduced at higher flow rates, thus allowing a higher overall

480   quantity of toluene to be degraded. Nevertheless, the total amount of mass degraded in 30 minutes

481   when the flow rate was fixed at 225 sL/h, that is 2.69 mg, is similar to the one measured for flow rate

482   fixed at 300 sL/h, that is 2.7 mg.

483   By adjusting it by time and photocatalyst surface area, we can therefore hypothesize a flow rate-

484   independent limit of degradable toluene equal to 0.9 $mg \cdot min^{-1} \cdot m^{-2}$ for an inlet toluene concentration

485   of 10 ppm. The analysis of the actual degraded quantity is often neglected or not reported in the

486   literature; however, it allows to better evaluate the real efficiency of a photocatalytic system.

487

488
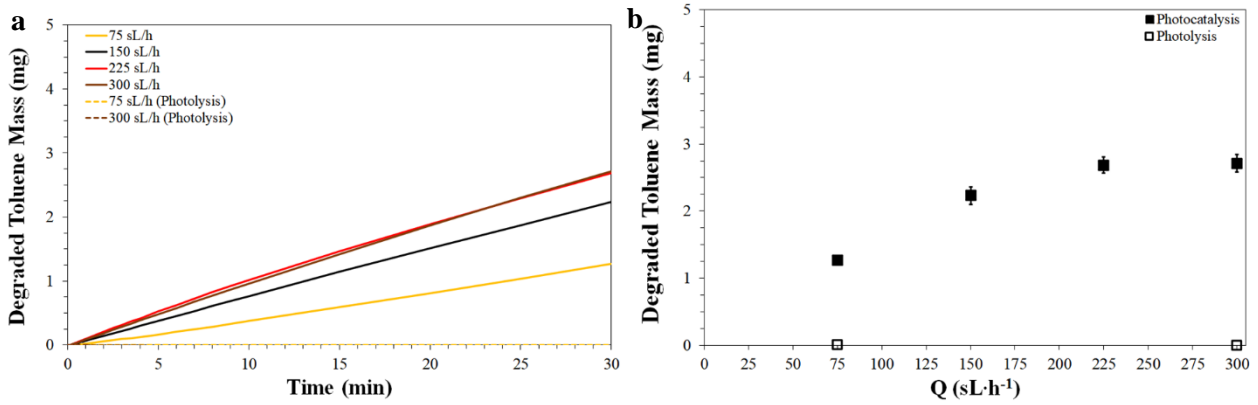
Figure 8. (a) Cumulative degraded toluene mass upon UV light illumination; (b) Overall degraded

mass as function of flow rate.

491

The obtained results also allow to evaluate the kinetics of the photodegradation process. Generally, it

is assumed that the adsorption of the pollutant on the photocatalyst surface is the rate-determining

step in the photocatalytic oxidation process, being the competitive water adsorption process less

influent [36]. However, toluene photocatalytic degradation involves a complex reaction mechanism

by generating several by-products, mainly benzaldehyde, that may strongly adsorb on the surface.

Therefore, a more simplistic L-H adsorption kinetic model was used for the reaction rate analysis,

which has been widely adopted by several researchers [4,48,54].

By using Eq. (7) based on L-H model and by considering C as the outlet concentration after 30

minutes of UV irradiation, a plot $\ln(C_{in}/C_{out})/(C_{in}-C_{out})$ versus $\tau/(C_{in}-C_{out})$ can be obtained, as shown

in Figure 9. If the model is valid, the regression analysis should be linear.

502

503
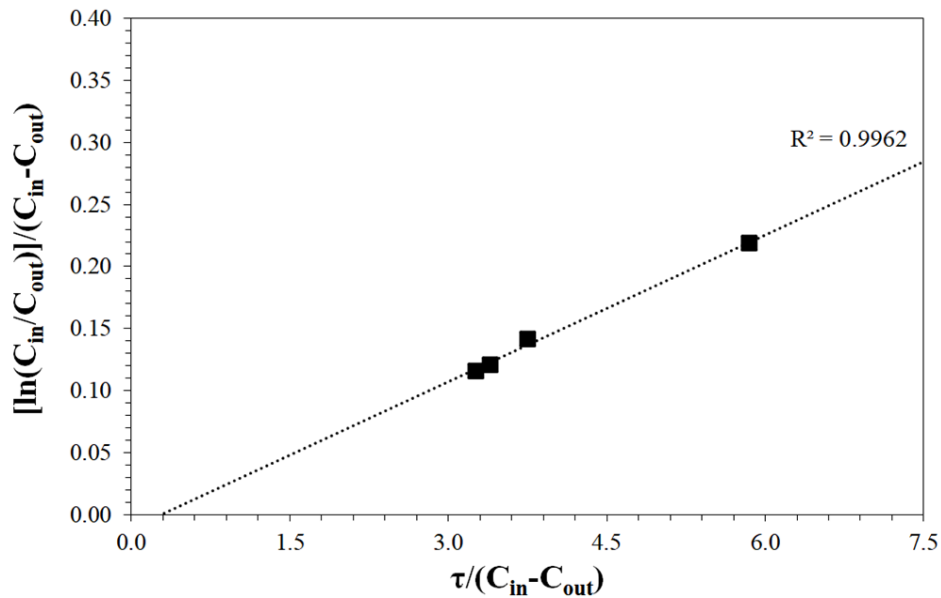
Figure 9. Regression analysis obtained by using the kinetic model of Eq. (7).

505

506 The performed regression analysis shows a high linearity, being R^2 equal to 0.9962, confirming that

507 the simplified L-H model can properly describe toluene photocatalytic degradation at low

508 concentrations.

509 The linear approximation is characterized by a slope equal to 0.039 and an intercept of -0.011; these

510 last one can be directly correlated to the adsorption constant K_{LH}, that reflects the photocatalyst

511 surface coverage of the pollutant (Eq. (7)); hence, K_{LH} is equal to 0.011 $m^3 \cdot g^{-1}$. Moreover, according

512 to Eq. (7), the slope is equal to kK_{LH}, that is, the product of reaction rate constant and adsorption

513 constant, giving a value of k equal to 3.55 $g \cdot m^{-3} \cdot s^{-1}$.

514 Results show that the influence of the adsorption constant is very low in the evaluated conditions. It

515 must be pointed out that, even if the degradation rate is strictly dependent on both k and K_{LH}, a low

516 adsorption constant does not involve a low toluene conversion [4,54].

517 By considering that both K_{LH} and pollutant concentration are very low ($K_{LH}C \ll 1$), the reaction rate

518 can be expressed through a pseudo-first-order kinetic model, as shown in Eq. (8).

519 Linearization of $ln(C_{out}/C_{in})$ versus residence time is reported in Figure 10.

520
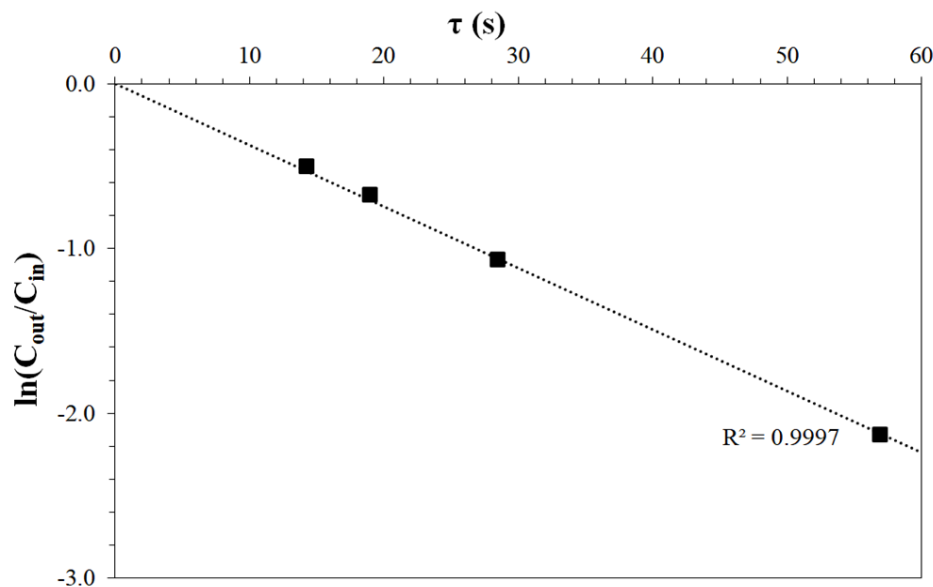
Figure 10. First-order kinetics of the RhB photocatalytic degradation process.

The resulting regression analysis shows a high linearity ($R^2 = 0.9997$), suggesting that the assumption of simplified L-H model for low concentrated pollutants properly describes the photocatalytic degradation of toluene. Moreover, the apparent reaction rate constant k_{app}, that is, the slope of the regression equation, is equal to 0.037 s^{-1} similarly to the previously found kK_{LH} equal to 0.039 s^{-1}; this confirms that K_{LH} is sufficiently low to be considered negligible.

Furthermore, the obtained results show that the pseudo-first-order assumptions used to describe the photocatalytic degradation in liquid phase are still valid for the kinetics description of gas phase pollutants; thus, an increase in k_{app} would involve a higher removal of the VOC. Eventually, the validation of this model allow to confirm the mass transfer is not the limiting step in the photocatalytic degradation process of toluene by using this built-in plug flow reactor.

However, it must be pointed out that L-H model for gas phase pollutants is generally restricted to the analysis of the initial photocatalytic degradation rate due to the complex reaction mechanism that involves the generation of by-products [55]; thus, the above considerations are not automatically valid for long term analyses (reaction time higher than 60 minutes).

539   3.3.2. High concentration

540   The effect of toluene concentration was evaluated by fixing relative humidity (RH = 50%) and flow

541   rate (150 sL/h), and by varying inlet concentration (20, 35 and 80 ppm, respectively). All experiments

542   were conducted for 360 min.

543   Toluene concentration profiles recorded in dark storage for 30 minutes and for the first 30 minutes

544   after photocatalyst activation are reported in Figure 11a. Results show that concentration profiles

545   remain constant in dark environment, whereas a concentration decrease is measured after UV-A lamp

546   is switched on. Being the rates of both photolysis (Figure S5) and adsorption in dark negligible,

547   photocatalytic degradation is considered the main responsible of the concentration decrease observed.

548   Although the initial toluene degradation percentage observed in the first minutes of irradiation is in

549   all cases between 60 and 70% (Figure 11b), at the highest inlet concentration the instant degradation

550   shows an evident gradual decrease after reaching this maximum condition. Hence, the maximum

551   percent degradation occurring at the beginning of the test is not sufficient to evaluate possible

552   applications in environments with high VOCs concentrations, as this value is not maintained in time;

553   for this reason, photocatalyst was exposed for six hours to toluene streams at different concentrations.

554
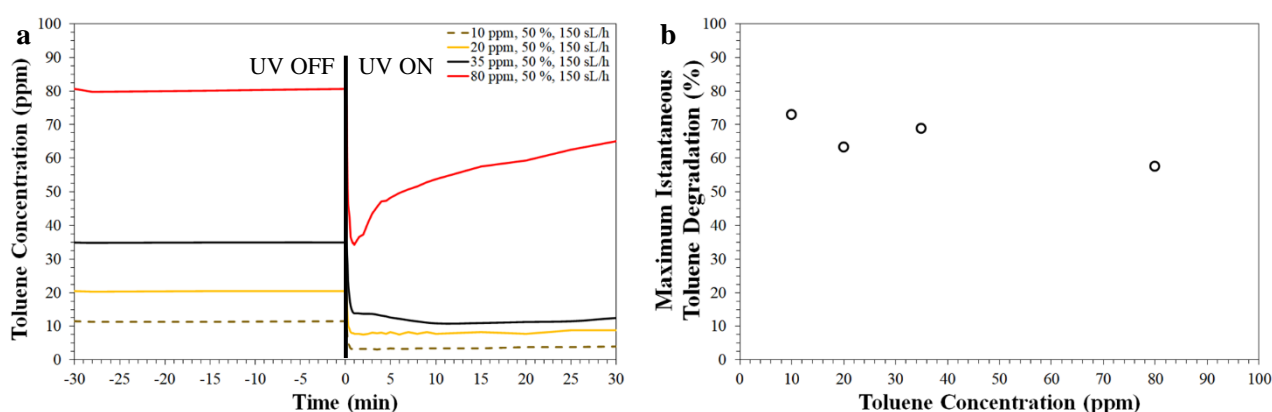
555

556   Figure 11. (a) Toluene concentration profile before and during UV-A irradiation (measured for 30

557   minutes); (b) maximum instant toluene conversion reached at different inlet toluene concentrations.

558

559 Toluene concentration profiles and instant degradation percentages recorded for a period of 6 hours

560 are reported in Figure 12. Results clearly show that instant degradation extents at high toluene inlet

561 concentrations decrease over six hours; in particular, for an inlet of concentration of 80 ppm the inlet

562 and outlet toluene concentration values equal – i.e., toluene degradation stops – after less than 60

563 minutes, suggesting a possible de-activation. Complete loss of degradation capability is reached also

564 at lower inlet concentrations, but in longer times.
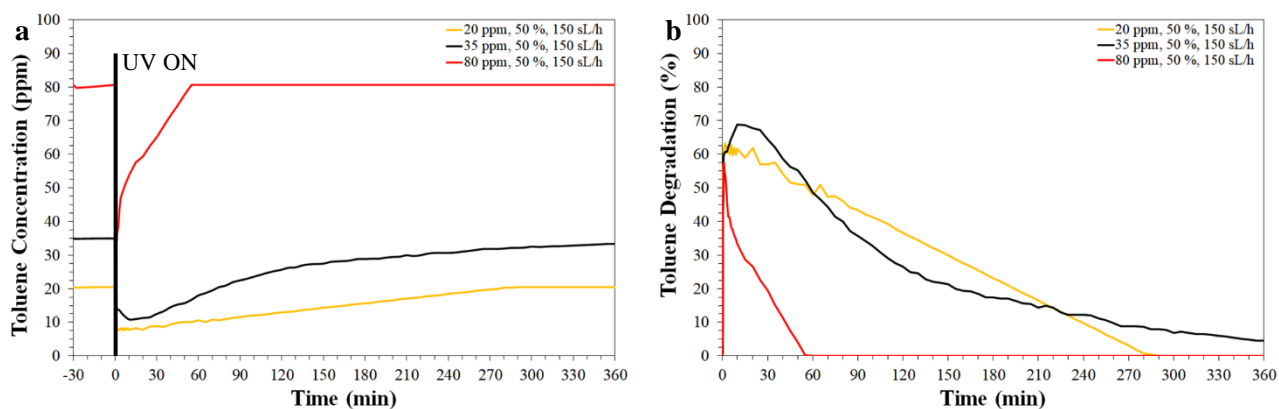
566 Figure 12. (a) Toluene concentration profile (a) and toluene conversion (b) upon UV light

567 illumination for 360 minutes.

568

569 Figure 13 shows the degraded mass profiles evaluated by applying Eq. (3); results show that the total

570 mass is strongly affected by inlet toluene concentration. In particular, after 30 minutes of UV-A

571 exposure the total degraded mass increases with inlet concentration increasing from 20 to 35 ppm,

572 then stabilizing in a range 6.5 – 6.6 mg also at an inlet concentration of 80 ppm.

573 Apparently, independently on inlet concentration, a limit of degradable toluene equal to of 2.08

574 $mg \cdot min^{-1} \cdot m^{-2}$ in the first 30 minutes irradiation can be assumed. This timeframe was chosen since

575 after 30 min the photocatalyst is not completely de-activated yet, while for longer times the overall

576 degraded mass depends on photocatalyst de-activation rate, which is faster for the highest inlet

577 concentration tested. This led to very low overall degraded mass at 80 ppm inlet concentration, while

578 at 20 and 35 ppm degradation slowly continued, leading to better results.
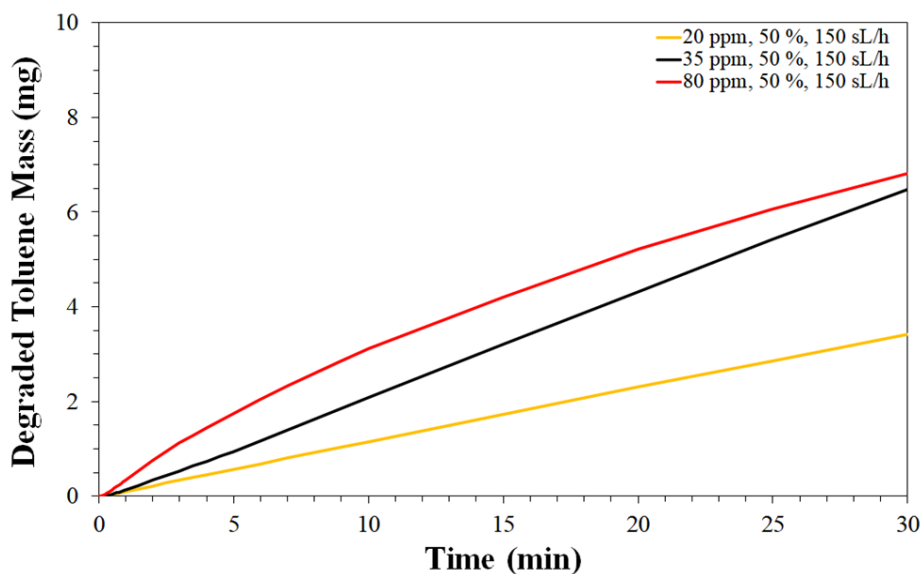
Figure 13. Toluene degraded mass profile as a function of irradiation time.

This can be ascribed to the fact that for very high concentration the amount of hydroxyl radicals generated during the photocatalytic test is not sufficient to withstand both the incoming toluene concentration and the large amount of by-products that are instantaneously formed and adsorbed at the photocatalyst surface, leading to a fast complete saturation. On the opposite, lower concentrations allow at least part of reaction sites to remain active for longer times, leading to the overall degradation of a higher amount of toluene.

To evaluate by-products formation, the outlet gas stream was examined by GC-MS. Sampling performed in dark environment and after 2 and 30 minutes of UV-A irradiation allowed to identify only toluene, whereas gas-phase intermediate organic products were not detected (see Supplementary Material, Figure S7-S9). NDIR analyses also gave non-relevant results, as the amount of CO_2 produced by the photocatalytic toluene oxidation was not distinguishable from the background signal. Tests were performed also during reactor cleaning (see Par. 3.3.4), and gave identical results. This was ascribed to intermediates exiting the reactor only in traces, i.e., not detectable with the equipment used, as they were also degraded in the photoreactor before being released.

596   For these reasons, the photocatalytic degradation pathway was assessed by analyzing adsorbed

597   byproducts on TiO₂ surface through FT-IR spectroscopy.

598
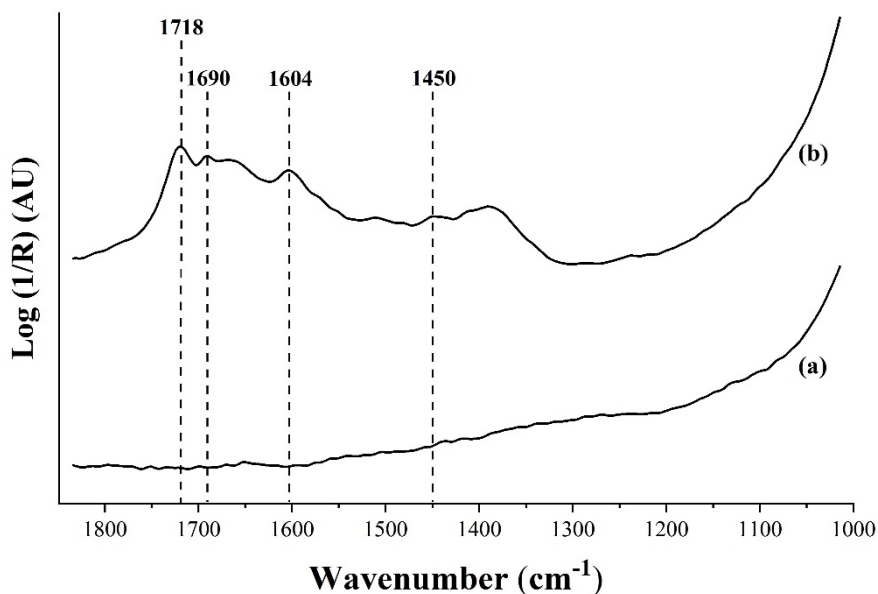
599

600   Figure 14. FT-IR spectra of byproducts adsorbed on TiO₂ surface (in presence of toluene with an inlet

601   concentration of 80 ppm, RH = 50% and flow rate of 150 sL/h): (a) before irradiation; (b) after 6 hour

602   irradiation.

603

604   Figure 14 shows infrared spectra performed on the photocatalyst surface before and after UV-A

605   irradiation, respectively.

606   Indeed, after 6 h irradiation small peaks can be identified at 1604, 1690 and 1718 cm^{-1}, which were

607   assigned to C=C stretching (aromatic ring vibrational mode) and C=O stretching, respectively [56–

608   61]. The small peak at 1450 cm^{-1} was also assigned to C=C stretching. These signals are compatible

609   with the possible adsorption of benzaldehyde, one of the most poisoning by-products of toluene

610   photocatalytic degradation [62–64].

611   It is then possible to hypothesize that benzaldehyde formed during toluene photocatalytic oxidation

612   strongly adsorbs at the photocatalyst surface and occupies adsorption sites that should have been

613 available to both water vapor and toluene, thus leading to a progressive de-activation of TiO_2 during

614 the process.

615 However, peaks intensity is rather low, therefore other reaction by-products of toluene and

616 benzaldehyde may be present in smaller quantities, such as benzoic acid [63–65], contributing to the

617 deactivation of the photocatalyst itself.

618

619 3.3.3. Effect of relative humidity

620 The effect of relative humidity on the photocatalytic degradation of toluene was evaluated at two

621 different pollutant concentrations (20 ppm and 30 ppm), by fixing inlet flow rate (150 sL/h) and by

622 varying the relative humidity of the inlet flow.

623 Three different relative humidity levels were selected, 25%, 50% and 75%; experiments were

624 conducted for a period of 120 min to better evaluate the effects of humidity in the medium term

625 (Figure 15).

626 Tests performed at 30 ppm immediately show an increase in the concentration profile, which can be

627 associated to a strong accumulation of by-products after some minutes of UV-A irradiation. As

628 previously described, an increase in the toluene concentration profile is linked to the de-activation of

629 the photocatalyst. The same effect is observed at 20 ppm with low relative humidity (25%), while at

630 higher relative humidity the instant degradation decreases at a lower speed, thus reducing the negative

631 consequences of de-activation, probably on account of a better surface coverage with OH• radicals.

632

633
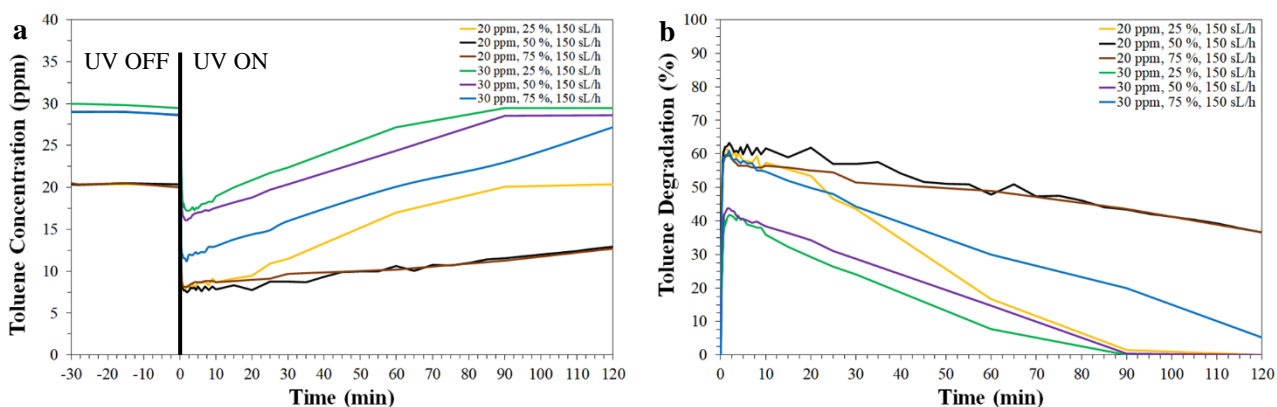
Figure 15. (a) Toluene concentration profile (a) and toluene conversion (b) upon UV-A irradiation at different relative humidity levels for an inlet concentration of 20 and 30 ppm.

Results indicate a partially beneficial effect of relative humidity, but only in the less stringent circumstances (highest RH, lowest inlet toluene concentration). Indeed, different authors reported that an increase in humidity may not affect photocatalytic degradation of toluene [66] or could decrease it [67,68], as an excessive RH level may cause competitive adsorption between water and pollutant on the photocatalyst surface, thus reducing the pollutant conversion [11].

However, this competitive mechanism may be favorable in case of toluene photocatalytic degradation: an increase in adsorbed water on TiO_2 may retard the accumulation of benzaldehyde and other by-products on the photocatalyst surface, thus hindering its de-activation.

3.3.4. Photocatalyst regeneration

As previously mentioned, the photocatalyst was subjected to a cleaning cycle lasting 60 minutes after each experiment. It was performed by stopping the VOC stream and letting synthetic air at high relative humidity level (in a range 50-75%) flow inside the reactor; during this step, UV-A lamp was left turned on to favor the removal of adsorbed reaction byproducts. Subsequently, dry air was used for the removal of moisture inside the reaction chamber.

Although this cleaning cycle is relatively short and therefore practical for possible real and large-scale applications, traces of adsorbed by-products may remain on TiO_2 surface, especially after strong poisoning and consequent deactivation. For this reason, deep cleaning cycles for a rigorous re-activation of the photocatalyst were performed by flowing synthetic air at high relative humidity level (in a range 50-75%) under UV-A irradiation for 24 hours. The effects of deep cleaning cycle were investigated by performing tests at fixed toluene concentration (20 ppm) and fixed flow rate (150 sL/h) at three different relative humidity levels, namely 25%, 50% and 75%; the 24-hours cleaning cycle was performed between consecutive tests.

660 Figure 16 shows toluene concentration profiles recorded for a period of 2 hours. Results clearly show

661 an increase in toluene degradation with respect to tests performed with the 60-minutes cleaning cycle.

662 Even more, the effect of relative humidity seems less evident, being the toluene concentration profiles

663 highly overlapping throughout the duration of the test.

664
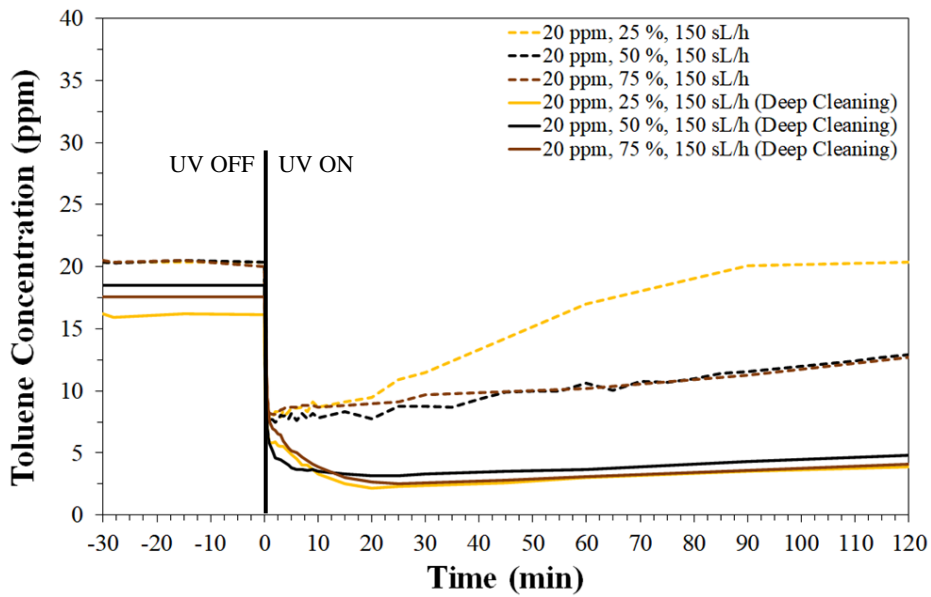
666 Figure 16. Toluene concentration profile upon UV light illumination for 120 minutes.

667
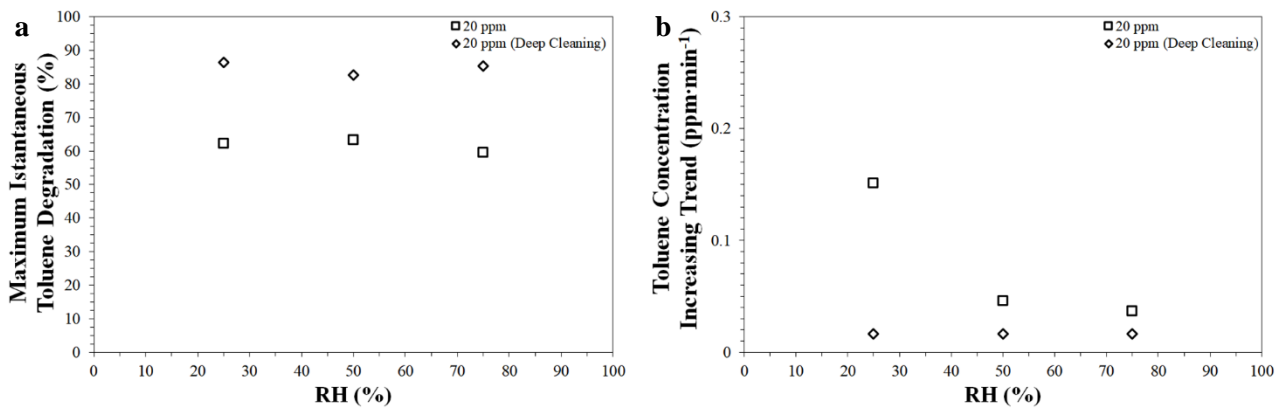
669 Figure 17. Effects of relative humidity and deep cleaning cycle on maximum instantaneous toluene

670 degradation (a) and toluene concentration increasing trend (b).

671

672   Moreover, an increase in maximum instant degradation percentage is observed in the whole range of

673   relative humidity level, up to 90 % of toluene degradation (Figure 17a).

674   Even with a deep cleansing cycle an increase in toluene concentration profile was observed after

675   reaching the maximum degradation, although delayed. However, the deep cleaning cycle ensures a

676   slower growth trend in concentration than that measured after a quick cleaning cycle, and the

677   difference is marked especially at low humidity levels, with a difference in slopes of more than one

678   order of magnitude (Figure 17b).

679   These results show that the deactivation observed is reversible, and that regeneration through a long-

680   term cleaning cycle can be performed by simply using UV-A radiation and a stream of moist air, a

681   simpler and cheaper technology than those often used for TiO_2 photocatalysts, such as calcination

682   [66] or use of oxidizing chemicals [4].

683

684

685   4. CONCLUSION

686   In this work, a prototype of annular photocatalytic reactor is proposed, using self-assembled

687   TiO_2 nanotubes as photocatalyst and a 15 W UV-A black-light bulb lamp, which demonstrated to be

688   efficient in the degradation of toluene as a model VOC. The high exposed surface area allows to

689   degrade up to 90% toluene with an inlet concentration of 10 ppm, flow rate 75 sL/h; slightly lower

690   efficiencies in terms of percent degradation were achieved at higher flow rates due to the lower

691   residence time in the reactor. Still, in the range of conditions tested we have found a flow rate-

692   independent limit of degradable toluene equal to 0.9 mg·min^{-1}·m^{-2}, thus resulting applicable for the

693   purification of moderately polluted air. We have demonstrated the feasibility of a device capable of

694   achieving high efficiency without resorting to the use of TiO_2 nanoparticles, whose release in the

695   environment is potentially hazardous.

696   The reactor was tested also at higher concentrations of toluene, leading to relatively high mass of

697   toluene converted in the first minutes of test, then followed by a gradual photocatalyst deactivation;

698 indeed, toluene degradation intermediates such as benzaldehyde contaminate the photocatalyst as the

699 reaction proceeds. Nonetheless, a regeneration treatment carried out using a flow of synthetic air and

700 water vapor under the same UV-A irradiation of normal tests was able to re-activate the photocatalyst

701 without involving hazardous chemicals or reactor disassembly.

702

703 ACKNOWLEDGEMENT

704

706

707

708

709

710 REFERENCES

711

712 [1]   I. Paciência, J. Madureira, J. Rufo, A. Moreira, E. de O. Fernandes, A systematic review of

713   evidence and implications of spatial and seasonal variations of volatile organic compounds

714   (VOC) in indoor human environments, J. Toxicol. Environ. Heal. - Part B Crit. Rev. 19

715   (2016) 47–64. https://doi.org/10.1080/10937404.2015.1134371.

716 [2]   I. Manisalidis, E. Stavropoulou, A. Stavropoulos, E. Bezirtzoglou, Environmental and Health

717   Impacts of Air Pollution: A Review, Front. Public Heal. 8 (2020) 1–13.

718   https://doi.org/10.3389/fpubh.2020.00014.

719 [3]   G.H. Pandya, V.K. Kondawar, A.G. Gavane, An integrated investigation of volatile organic

720   compounds emission in the atmosphere from refinery and its off-site facilities, Indian J.

721   Chem. Technol. 14 (2007) 283–291.

722 [4]   R.M. Alberici, W.F. Jardim, Photocatalytic destruction of VOCS in the gas-phase using

723   titanium dioxide, Appl. Catal. B Environ. 14 (1997) 55–68. https://doi.org/10.1016/S0926-

724   3373(97)00012-X.

725 [5] E. Bustaffa, A. De Marinis Loiotile, G. Farella, S. Petraccone, G. De Gennaro, F. Bianchi,

726   Idrocarburi non metanici nell'atmosfera in prossimità di impianti di primo trattamento del

727   greggio, Epidemiol. Prev. 40 (2016) 290–306. https://doi.org/10.19191/EP16.5.P290.104.

728 [6] H. Rajabi, M.H. Mosleh, P. Mandal, A. Lea-Langton, M. Sedighi, Emissions of volatile

729   organic compounds from crude oil processing – Global emission inventory and

730   environmental release, Sci. Total Environ. 727 (2020) 138654.

731   https://doi.org/10.1016/j.scitotenv.2020.138654.

732 [7] Y. Boyjoo, H. Sun, J. Liu, V.K. Pareek, S. Wang, A review on photocatalysis for air

733   treatment: From catalyst development to reactor design, Chem. Eng. J. 310 (2017) 537–559.

734   https://doi.org/10.1016/j.cej.2016.06.090.

735 [8] T.M. Fujimoto, M. Ponczek, U.L. Rochetto, R. Landers, E. Tomaz, Photocatalytic oxidation

736   of selected gas-phase VOCs using UV light, TiO_2, and TiO_2/Pd, Environ. Sci. Pollut. Res.

737   24 (2017) 6390–6396. https://doi.org/10.1007/s11356-016-6494-7.

738 [9] C.A. Korologos, M.D. Nikolaki, C.N. Zerva, C.J. Philippopoulos, S.G. Poulopoulos,

739   Photocatalytic oxidation of benzene, toluene, ethylbenzene and m-xylene in the gas-phase

740   over TiO_2-based catalysts, J. Photochem. Photobiol. A Chem. 244 (2012) 24–31.

741   https://doi.org/10.1016/j.jphotochem.2012.06.016.

742 [10] Y.H. Li, S.W. Cheng, C.S. Yuan, T.F. Lai, C.H. Hung, Removing volatile organic

743   compounds in cooking fume by nano-sized TiO_2 photocatalytic reaction combined with

744   ozone oxidation technique, Chemosphere. 208 (2018) 808–817.

745   https://doi.org/10.1016/j.chemosphere.2018.06.035.

746 [11] G. Vincent, P.M. Marquaire, O. Zahraa, Abatement of volatile organic compounds using an

747   annular photocatalytic reactor: Study of gaseous acetone, J. Photochem. Photobiol. A Chem.

748   197 (2008) 177–189. https://doi.org/10.1016/j.jphotochem.2007.12.021.

749 [12] R. López-Fonseca, B. De Rivas, J.I. Gutiérrez-Ortiz, A. Aranzabal, J.R. González-Velasco,

750   Enhanced activity of zeolites by chemical dealumination for chlorinated VOC abatement,

751   Appl. Catal. B Environ. 41 (2003) 31–42. https://doi.org/10.1016/S0926-3373(02)00199-6.

752 [13] A. Jantschak, M. Daniels, R. Paschold, Biofilter technology: An innovative and cost-

753   effective system to remove VOC, IEEE Trans. Semicond. Manuf. 17 (2004) 255–260.

754   https://doi.org/10.1109/TSM.2004.831936.

755 [14] J. Brunet, E. Genty, Y. Landkocz, M. Al Zallouha, S. Billet, D. Courcot, S. Siffert, D.

756   Thomas, G. De Weireld, R. Cousin, Identification of by-products issued from the catalytic

757   oxidation of toluene by chemical and biological methods, Comptes Rendus Chim. 18 (2015)

758   1084–1093. https://doi.org/10.1016/j.crci.2015.09.001.

759 [15] V. Binas, D. Venieri, D. Kotzias, G. Kiriakidis, Modified TiO2 based photocatalysts for

760   improved air and health quality, J. Mater. 3 (2017) 3–16.

761   https://doi.org/10.1016/j.jmat.2016.11.002.

762 [16] M.S. Kamal, S.A. Razzak, M.M. Hossain, Catalytic oxidation of volatile organic compounds

763   (VOCs) - A review, Atmos. Environ. 140 (2016) 117–134.

764   https://doi.org/10.1016/j.atmosenv.2016.05.031.

765 [17] V. Dal Santo, A. Naldoni, Titanium dioxide photocatalysis, Catalysts. 8 (2018) 10–13.

766   https://doi.org/10.3390/catal8120591.

767 [18] A.J. Haider, Z.N. Jameel, I.H.M. Al-Hussaini, Review on: Titanium dioxide applications,

768   Energy Procedia. 157 (2019) 17–29. https://doi.org/10.1016/j.egypro.2018.11.159.

769 [19] C. Byrne, G. Subramanian, S.C. Pillai, Recent advances in photocatalysis for environmental

770   applications, J. Environ. Chem. Eng. 6 (2018) 3531–3555.

771   https://doi.org/10.1016/j.jece.2017.07.080.

772 [20] M.V. Diamanti, M. Ormellese, M.P. Pedeferri, Application-wise nanostructuring of anodic

773   films on titanium: a review, J. Exp. Nanosci. 10 (2015) 1285–1308.

774   https://doi.org/10.1080/17458080.2014.999261.

775 [21] M.V. Diamanti, B. del Curto, M. Pedeferri, Anodic oxidation of titanium: From technical

776   aspects to biomedical applications, J. Appl. Biomater. Biomech. 9 (2011) 55–69.

777   https://doi.org/10.5301/JABB.2011.7429.

778   [22]   E. Poulakis, C. Philippopoulos, Photocatalytic treatment of automotive exhaust emissions,

779   Chem. Eng. J. 309 (2017) 178–186. https://doi.org/10.1016/j.cej.2016.10.030.

780   [23]   R.A.R. Monteiro, S.M. Miranda, C. Rodrigues-Silva, J.L. Faria, A.M.T. Silva, R.A.R.

781   Boaventura, V.J.P. Vilar, Gas phase oxidation of n-decane and PCE by photocatalysis using

782   an annular photoreactor packed with a monolithic catalytic bed coated with P25 and PC500,

783   Appl. Catal. B Environ. 165 (2015) 306–315. https://doi.org/10.1016/j.apcatb.2014.10.026.

784   [24]   B.M. Rao, A. Torabi, O.K. Varghese, Anodically grown functional oxide nanotubes and

785   applications, MRS Commun. 6 (2016) 375–396. https://doi.org/10.1557/mrc.2016.46.

786   [25]   Y. Feng, H.H.M. Rijnaarts, D. Yntema, Z. Gong, D.D. Dionysiou, Z. Cao, S. Miao, Y. Chen,

787   Y. Ye, Y. Wang, Applications of anodized TiO2 nanotube arrays on the removal of aqueous

788   contaminants of emerging concern: A review, Water Res. 186 (2020) 116327.

789   https://doi.org/10.1016/j.watres.2020.116327.

790   [26]   Y.C. Nah, I. Paramasivam, P. Schmuki, Doped TiO2 and TiO2 nanotubes: Synthesis and

791   applications, ChemPhysChem. 11 (2010) 2698–2713.

792   https://doi.org/10.1002/cphc.201000276.

793   [27]   H. Li, Z. Chen, C.K. Tsang, Z. Li, X. Ran, C. Lee, B. Nie, L. Zheng, T. Hung, J. Lu, B. Pan,

794   Y.Y. Li, Electrochemical doping of anatase TiO2 in organic electrolytes for high-

795   performance supercapacitors and photocatalysts, J. Mater. Chem. A. 2 (2014) 229–236.

796   https://doi.org/10.1039/c3ta13963h.

797   [28]   Y. Dou, X. Feng, C. Yin, N-doped TiO2 nanotubes and its photocatalytic activity under UV

798   light, Adv. Mater. Res. 156–157 (2011) 1725–1729.

799   https://doi.org/10.4028/www.scientific.net/AMR.156-157.1725.

800   [29]   I. Ali, K. Park, S.R. Kim, J.O. Kim, Electrochemical anodization of graphite oxide-TiO 2

801   nanotube composite for enhanced visible light photocatalytic activity, Environ. Sci. Pollut.

802   Res. 26 (2019) 1072–1081. https://doi.org/10.1007/s11356-017-8571-y.

803   [30] U. Bellè, F. Pelizzari, A. Lucotti, C. Castiglioni, M. Ormellese, M. Pedeferri, M.V. Diamanti,

804   Immobilized nano-tio2 photocatalysts for the degradation of three organic dyes in single and

805   multi-dye solutions, Coatings. 10 (2020) 1–23. https://doi.org/10.3390/coatings10100919.

806   [31] H. Sopha, M. Baudys, M. Krbal, R. Zazpe, J. Prikryl, J. Krysa, J.M. Macak, Scaling up

807   anodic TiO2 nanotube layers for gas phase photocatalysis, Electrochem. Commun. 97 (2018)

808   91–95. https://doi.org/10.1016/j.elecom.2018.10.025.

809   [32] A.G. Kontos, A. Katsanaki, T. Maggos, V. Likodimos, A. Ghicov, D. Kim, J. Kunze, C.

810   Vasilakos, P. Schmuki, P. Falaras, Photocatalytic degradation of gas pollutants on self-

811   assembled titania nanotubes, Chem. Phys. Lett. 490 (2010) 58–62.

812   https://doi.org/10.1016/j.cplett.2010.03.009.

813   [33] A.G. Kontos, A. Katsanaki, V. Likodimos, T. Maggos, D. Kim, C. Vasilakos, D.D.

814   Dionysiou, P. Schmuki, P. Falaras, Continuous flow photocatalytic oxidation of nitrogen

815   oxides over anodized nanotubular titania films, Chem. Eng. J. 179 (2012) 151–157.

816   https://doi.org/10.1016/j.cej.2011.10.072.

817   [34] Y. Qin, Z. Wang, J. Jiang, L. Xing, K. Wu, One-step fabrication of TiO2/Ti foil annular

818   photoreactor for photocatalytic degradation of formaldehyde, Chem. Eng. J. 394 (2020)

819   124917. https://doi.org/10.1016/j.cej.2020.124917.

820   [35] I. Grčić, J. Marčec, L. Radetić, A.M. Radovan, I. Melnjak, I. Jajčinović, I. Brnardić,

821   Ammonia and methane oxidation on TiO2 supported on glass fiber mesh under artificial

822   solar irradiation, Environ. Sci. Pollut. Res. 28 (2021) 18354–18367.

823   https://doi.org/10.1007/s11356-020-09561-y.

824   [36] V. Tomašić, F. Jović, Z. Gomzi, Photocatalytic oxidation of toluene in the gas phase:

825   Modelling an annular photocatalytic reactor, Catal. Today. 137 (2008) 350–356.

826   https://doi.org/10.1016/j.cattod.2008.05.017.

827   [37] T.H. Lim, S.D. Kim, Trichloroethylene degradation by photocatalysis in annular flow and

828   annulus fluidized bed photoreactors, Chemosphere. 54 (2004) 305–312.

829   https://doi.org/10.1016/S0045-6535(03)00753-7.

830   [38] J.M. Macak, H. Tsuchiya, A. Ghicov, K. Yasuda, R. Hahn, S. Bauer, P. Schmuki, TiO2

831   nanotubes: Self-organized electrochemical formation, properties and applications, Curr.

832   Opin. Solid State Mater. Sci. 11 (2007) 3–18. https://doi.org/10.1016/j.cossms.2007.08.004.

833   [39] O.K. Varghese, D. Gong, M. Paulose, C.A. Grimes, E.C. Dickey, Crystallization and high-

834   temperature structural stability of titanium oxide nanotube arrays, J. Mater. Res. 18 (2003)

835   156–165. https://doi.org/10.1557/JMR.2003.0022.

836   [40] F.V.S. Lopes, R.A.R. Monteiro, A.M.T. Silva, G. V. Silva, J.L. Faria, A.M. Mendes, V.J.P.

837   Vilar, R.A.R. Boaventura, Insights into UV-TiO2 photocatalytic degradation of PCE for air

838   decontamination systems, Chem. Eng. J. 204–205 (2012) 244–257.

839   https://doi.org/10.1016/j.cej.2012.07.079.

840   [41] F. Khodadadian, M.W. de Boer, A. Poursaeidesfahani, J.R. van Ommen, A.I. Stankiewicz, R.

841   Lakerveld, Design, characterization and model validation of a LED-based photocatalytic

842   reactor for gas phase applications, Chem. Eng. J. 333 (2018) 456–466.

843   https://doi.org/10.1016/j.cej.2017.09.108.

844   [42] N. Blommaerts, R. Asapu, N. Claes, S. Bals, S. Lenaerts, S.W. Verbruggen, Gas phase

845   photocatalytic spiral reactor for fast and efficient pollutant degradation, Chem. Eng. J. 316

846   (2017) 850–856. https://doi.org/10.1016/j.cej.2017.02.038.

847   [43] H. Il Kim, D. Kim, W. Kim, Y.C. Ha, S.J. Sim, S. Kim, W. Choi, Anodic TiO2 nanotube

848   layer directly formed on the inner surface of Ti pipe for a tubular photocatalytic reactor,

849   Appl. Catal. A Gen. 521 (2016) 174–181. https://doi.org/10.1016/j.apcata.2015.10.039.

850   [44] W.M. Hou, Y. Ku, Photocatalytic decomposition of gaseous isopropanol in a tubular optical

851   fiber reactor under periodic UV-LED illumination, J. Mol. Catal. A Chem. 374–375 (2013)

852   7–11. https://doi.org/10.1016/j.molcata.2013.03.016.

853   [45] B.E.S. Arenas, A. Strini, L. Schiavi, A.L. Bassi, V. Russo, B. Del Curto, M.V. Diamanti,

854   M.P. Pedeferri, Photocatalytic activity of nanotubular TiO2 films obtained by anodic

855   oxidation: A comparison in gas and liquid phase, Materials (Basel). 11 (2018).

856   https://doi.org/10.3390/ma11040488.

857 [46] T.T. Shih, I.H. Hsu, J.F. Wu, C.H. Lin, Y.C. Sun, Development of chip-based photocatalyst-

858   assisted reduction device to couple high performance liquid chromatography and inductively

859   coupled plasma-mass spectrometry for determination of inorganic selenium species, J.

860   Chromatogr. A. 1304 (2013) 101–108. https://doi.org/10.1016/j.chroma.2013.06.067.

861 [47] T.A. McMurray, J.A. Byrne, P.S.M. Dunlop, E.T. McAdams, Photocatalytic and

862   electrochemically assisted photocatalytic oxidation of formic acid on TiO2 films under UVA

863   and UVB irradiation, J. Appl. Electrochem. 35 (2005) 723–731.

864   https://doi.org/10.1007/s10800-005-1397-1.

865 [48] A. Bouzaza, C. Vallet, A. Laplanche, Photocatalytic degradation of some VOCs in the gas

866   phase using an annular flow reactor: Determination of the contribution of mass transfer and

867   chemical reaction steps in the photodegradation process, J. Photochem. Photobiol. A Chem.

868   177 (2006) 212–217. https://doi.org/10.1016/j.jphotochem.2005.05.027.

869 [49] B. Kraeutler, A.J. Bard, OF THE, (1978).

870 [50] G. Odling, N. Robertson, Why is anatase a better photocatalyst than rutile? the importance of

871   free hydroxyl radicals, ChemSusChem. 8 (2015) 1838–1840.

872   https://doi.org/10.1002/cssc.201500298.

873 [51] Q.Y. Zeng, M. Xi, W. Xu, X.J. Li, Preparation of titanium dioxide nanotube arrays on

874   titanium mesh by anodization in (NH4)2SO4/NH4F electrolyte, Mater. Corros. 64 (2013)

875   1001–1006. https://doi.org/10.1002/maco.201106481.

876 [52] Z. Liu, Q. Zhang, T. Zhao, J. Zhai, L. Jiang, 3-D vertical arrays of TiO2 nanotubes on Ti

877   meshes: Efficient photoanodes for water photoelectrolysis, J. Mater. Chem. 21 (2011)

878   10354–10358. https://doi.org/10.1039/c1jm11072a.

879 [53] B. Chen, K. Lu, Influence of patterned concave depth and surface curvature on anodization

880   of titania nanotubes and alumina nanopores, Langmuir. 27 (2011) 12179–12185.

881   https://doi.org/10.1021/la202559h.

882   [54]   J. Palau, J.M. Penya-Roja, C. Gabaldón, F. Javier Álvarez-Hornos, F. Sempere, V. Martínez-

883   Soria, UV photocatalytic oxidation of paint solvent compounds in air using an annular TiO2-

884   supported reactor, J. Chem. Technol. Biotechnol. 86 (2011) 273–281.

885   https://doi.org/10.1002/jctb.2515.

886   [55]   S.B. Kim, S.C. Hong, Kinetic study for photocatalytic degradation of volatile organic

887   compounds in air using thin film TiO2 photocatalyst, Appl. Catal. B Environ. 35 (2002) 305–

888   315. https://doi.org/10.1016/S0926-3373(01)00274-0.

889   [56]   A.J. Maira, J.M. Coronado, V. Augugliaro, K.L. Yeung, J.C. Conesa, J. Soria, Fourier

890   transform infrared study of the performance of nanostructured TiO2 particles for the

891   photocatalytic oxidation of gaseous toluene, J. Catal. 202 (2001) 413–420.

892   https://doi.org/10.1006/jcat.2001.3301.

893   [57]   G. Martra, S. Coluccia, L. Marchese, V. Augugliaro, V. Loddo, L. Palmisano, M. Schiavello,

894   The role of H2O in the photocatalytic oxidation of toluene in vapour phase on anatase TiO2

895   catalyst A FTIR study, Catal. Today. 53 (1999) 695–702. https://doi.org/10.1016/S0920-

896   5861(99)00156-X.

897   [58]   G. Marcì, M. Addamo, V. Augugliaro, S. Coluccia, E. García-López, V. Loddo, G. Martra,

898   L. Palmisano, M. Schiavello, Photocatalytic oxidation of toluene on irradiated TiO2:

899   Comparison of degradation performance in humidified air, in water and in water containing a

900   zwitterionic surfactant, J. Photochem. Photobiol. A Chem. 160 (2003) 105–114.

901   https://doi.org/10.1016/S1010-6030(03)00228-4.

902   [59]   G. Martra, V. Augugliaro, S. Coluccia, E. García-López, V. Loddo, L. Marchese, L.

903   Palmisano, M. Schiavello, Photocatalytic oxidation of gaseous toluene on polycrystalline

904   TiO2: FT-IR investigation of surface reactivity of different types of catalysts, Stud. Surf. Sci.

905   Catal. 130 A (2000) 665–670. https://doi.org/10.1016/s0167-2991(00)81034-4.

906   [60]   X. Li, Z. Zhu, Q. Zhao, S. Liu, FT-IR study of the photocatalytic degradation of gaseous

907   toluene over UV-irradiated TiO 2 microballs: Enhanced performance by hydrothermal

908   treatment in alkaline solution, Appl. Surf. Sci. 257 (2011) 4709–4714.

909   https://doi.org/10.1016/j.apsusc.2010.12.133.

910   [61]   V. Augugliaro, S. Coluccia, V. Loddo, L. Marchese, G. Martra, L. Palmisano, M. Schiavello,

911   Photocatalytic oxidation of gaseous toluene on anatase TiO2 catalyst: Mechanistic aspects

912   and FT-IR investigation, Appl. Catal. B Environ. 20 (1999) 15–27.

913   https://doi.org/10.1016/S0926-3373(98)00088-5.

914   [62]   P.A. Deveau, F. Arsac, P.X. Thivel, C. Ferronato, F. Delpech, J.M. Chovelon, P. Kaluzny, C.

915   Monnet, Different methods in TiO2 photodegradation mechanism studies: Gaseous and

916   TiO2-adsorbed phases, J. Hazard. Mater. 144 (2007) 692–697.

917   https://doi.org/10.1016/j.jhazmat.2007.01.097.

918   [63]   C.L. Bianchi, S. Gatto, C. Pirola, A. Naldoni, A. Di Michele, G. Cerrato, V. Crocellà, V.

919   Capucci, Photocatalytic degradation of acetone, acetaldehyde and toluene in gas-phase:

920   Comparison between nano and micro-sized TiO2, Appl. Catal. B Environ. 146 (2014) 123–

921   130. https://doi.org/10.1016/j.apcatb.2013.02.047.

922   [64]   M. Sleiman, P. Conchon, C. Ferronato, J.M. Chovelon, Photocatalytic oxidation of toluene at

923   indoor air levels (ppbv): Towards a better assessment of conversion, reaction intermediates

924   and mineralization, Appl. Catal. B Environ. 86 (2009) 159–165.

925   https://doi.org/10.1016/j.apcatb.2008.08.003.

926   [65]   M. Le Bechec, N. Kinadjian, D. Ollis, R. Backov, S. Lacombe, Comparison of kinetics of

927   acetone, heptane and toluene photocatalytic mineralization over TiO2 microfibers and

928   Quartzel® mats, Appl. Catal. B Environ. 179 (2015) 78–87.

929   https://doi.org/10.1016/j.apcatb.2015.05.015.

930   [66]   U.R. Pillai, E. Sahle–Demessie, Selective Oxidation of Alcohols in Gas Phase Using Light-

931   Activated Titanium Dioxide, J. Catal. 211 (2002) 434–444.

932   https://doi.org/10.1006/jcat.2002.3771.

933   [67]   C.H. Ao, S.C. Lee, J.Z. Yu, J.H. Xu, Photodegradation of formaldehyde by photocatalyst

934   TiO2: Effects on the presences of NO, SO2 and VOCs, Appl. Catal. B Environ. 54 (2004)

935   41–50. https://doi.org/10.1016/j.apcatb.2004.06.004.

936   [68]   T. Maggos, J.G. Bartzis, P. Leva, D. Kotzias, Application of photocatalytic technology for

937   NOx removal, Appl. Phys. A Mater. Sci. Process. 89 (2007) 81–84.

938   https://doi.org/10.1007/s00339-007-4033-6.

939